

Nature of the Unidentified TeV Source HESS J1614–518, Revealed by Suzaku and XMM-Newton Observations

Michito SAKAI,¹ Yukie YAJIMA,¹ and Hironori MATSUMOTO²

¹*Division of Particle and Astrophysical Science, Graduate School of Science, Nagoya University,
Furo-cho, Chikusa-ku, Nagoya 464-8602*

m_sakai@u.phys.nagoya-u.ac.jp

²*Kobayashi-Maskawa Institute for the Origin of Particles and the Universe, Nagoya University,
Furo-cho, Chikusa-ku, Nagoya 464-8602*

(Received ; accepted)

Abstract

We report on new Suzaku and XMM-Newton results concerning HESS J1614–518, which is one of the brightest extended TeV γ -ray sources and has two regions with intense γ -ray emission. We newly observed the south and center regions of HESS J1614–518 with Suzaku, since the north region, including the position of the 1st brightest peak of the TeV γ -ray emission, has already been observed. No X-ray counterpart was found at the position of the 2nd brightest peak of the TeV γ -ray emission; we estimated the upper limit of the X-ray flux to be 1.6×10^{-13} erg cm⁻² s⁻¹ in the 2–10 keV band. The soft X-ray source Suzaku J1614–5152, which was found at the edge of the field of view in a previous observation, was also detected at the middle of HESS J1614–518. Analyzing the XMM-Newton archival data, we revealed that Suzaku J1614–5152 consists of multiple point sources. The X-ray spectrum of the brightest point source, XMMU J161406.0–515225, can be described by a power-law model with a photon index of $\Gamma = 5.2^{+0.6}_{-0.5}$, or a blackbody model with temperature $kT = 0.38^{+0.04}_{-0.04}$ keV. In the blackbody model, the hydrogen-equivalent column density is almost the same as that of the hard extended X-ray emission, Suzaku J1614–5141, which was found at the 1st peak position. If true, XMMU J161406.0–515225 may be physically related to Suzaku J1614–5141 and HESS J1614–518.

Key words: acceleration of particles — X-rays: individual (HESS J1614–518)

1. Introduction

Cosmic rays are the most energetic particles in the Universe. Since its discovery (Hess 1912), their origin has been a mystery. A large fraction of the Galactic cosmic rays reaching the earth are protons; only about 1% of those are electrons.

It has only been recently revealed that supernova remnants (SNRs) may be effective electron accelerators, as the detections of synchrotron X-rays originating from electrons with energies approaching $E \sim 10^{14}$ eV (e.g., Koyama et al. 1995). However, a clue for proton accelerators — constituting the majority of cosmic rays — evaded our eyes.

Then the progress has been made. The H.E.S.S. Cherenkov Telescope, a high-sensitivity TeV γ -ray telescope, has identified many very high energy (VHE) γ -ray objects along the Galactic plane (Aharonian et al. 2005a; Aharonian et al. 2005b). Most of the new objects are spatially extended and therefore be Galactic objects, such as pulsar wind nebulae (PWNe) (Renaud et al. 2008), shell-type SNRs (Aharonian et al. 2008), and binaries (Aharonian et al. 2005b), etc. Nevertheless, the nature of a large population of the VHE objects remains unknown. These unidentified sources have no clear counterpart at other wavelengths so that they are referred to as "dark particle accelerators" (Aharonian et al. 2005a). There are two possible mechanisms to radiate the VHE γ -rays efficiently: (1) electronic origin and (2) hadronic origin of γ -rays. In the former, VHE γ -rays results from inverse-Compton upscattering of seed photons (cosmic microwave background or other low-energy photons) by highly energized electrons — the same electrons which radiate X-rays in the synchrotron process. In the latter, VHE γ -rays are explained by the decay of neutral pions that originate in collisions between high-energy protons and dense interstellar matter. While TeV γ -ray emission may allude to the presence of high-energy particles, it does not differentiate the two possibilities. However, the presence of X-ray emission (or a lack of thereof) can shed a new light to the nature of these mysterious γ -ray sources.

HESS J1614–518 (hereafter HESS J1614) is one of the brightest, extended TeV γ -ray sources (Aharonian et al. 2005a; Aharonian et al. 2006). It has two regions with intense γ -ray emission. Since it has no viable counterpart identified in other wavelengths, HESS J1614 is considered as a dark particle accelerator.

Matsumoto et al. (2008) observed HESS J1614 in 2006 with Suzaku, an X-ray astronomical satellite (Mitsuda et al. 2007), to identify the TeV γ -ray source in X-rays. Two X-ray sources were found in the 3–10 keV band. One of the X-ray objects, Suzaku J1614–5141 (src A), is extended and is located very close to the position of the 1st brightest peak of the TeV γ -ray emission. The other source, Suzaku J1614–5152 (src B), is located at the middle of two TeV γ -ray peaks in HESS J1614. Detailed analysis of src B was proven difficult with the Suzaku observation in 2006 as the source resides near the edge of the field of view and its flux estimate suffers significant uncertainties. Hence the second Suzaku observation was conducted in 2008

in order to probe the nature of src B. We also observed the position of the 2nd brightest peak of the TeV γ -ray emission.

In the following sections, the results of the second Suzaku observation will be discussed; in addition, our own analysis on the XMM-Newton observation of the HESS J1614 region will be utilized to do a spatial analysis and to examine temporal behavior. The uncertainties in described parameters are at the 90% confidence level; the errors in data points and photon counts are at the 1σ level, unless otherwise stated.

2. Observations and Data Reduction

The south and center regions of HESS J1614 were observed on 2008 September 20 and 21, respectively. Figure 1 shows the Suzaku/X-ray Imaging Spectrometer (XIS: Koyama et al. 2007) field of views in these observations, together with that in the HESS J1614-North observation performed on 2006 September 16. The observations are summarized in table 1.

Suzaku consists of two distinct co-aligned scientific instruments. One is the X-ray Imaging Spectrometer (XIS: Koyama et al. 2007), which is an X-ray CCD camera located in the focal plane of the X-ray Telescope (XRT: Serlemitsos et al. 2007). The other is the Hard X-ray Detector (HXD: Kokubun et al. 2007; Takahashi et al. 2007), which is a non-imaging detector. The observations were performed with the three CCD cameras (XISs). One of the XIS sensors (XIS 1) has a back-illuminated (BI) CCD, while the other two (XISs 0 and 3) utilize front-illuminated (FI) CCDs. One of the FIs (XIS 2) suffered catastrophic damage on 2006 November 9, so that no useful data were obtained. The XIS was operated in the normal clocking mode (without the Burst or Window options) with the Spaced-row Charge Injection (SCI) (Uchiyama et al. 2009). The HXD data were also available.

We analyzed the data with the processing version of 2.2.11.22,¹ utilizing the HEADAS software (version 6.8) and the calibration database (CALDB) released on 2010 February 18. All data affected by the South Atlantic Anomaly and telemetry saturation were excluded. We excluded the data obtained with an elevation angle from the Earth rim of $< 5^\circ$. Additionally, for the XIS data, we also excluded the data obtained with that from the bright Earth rim of $< 20^\circ$ and removed hot/flickering pixels. After these data screenings, the effective exposures for the XIS data were 53.7 ks and 47.7 ks, and those for the HXD-PIN data were 40.9 ks and 43.0 ks, on the HESS J1614-South and the HESS J1614-Center, respectively.

3. Analysis and Results

3.1. XIS Image

We extracted XIS images from each sensor using the screened data for the soft- and hard-energy bands. For the FI sensors, the soft- and hard-bands are defined as 0.4–3 keV and 3–10

¹ See <http://www.astro.isas.jaxa.jp/suzaku/process/history/v221122.html>.

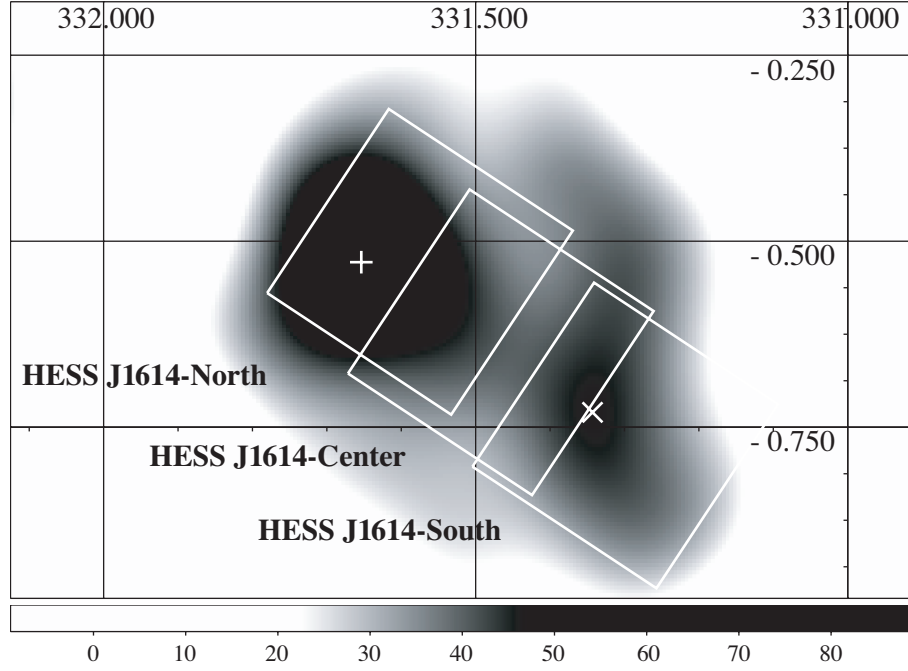


Fig. 1. Suzaku/XIS field of views (thick boxes) overlaid on the H.E.S.S. smoothed excess map. The scale bar below the figure represents the excess. The coordinates on the interior frame are Galactic. The plus and cross marks represent the positions of the 1st and 2nd brightest peaks of the TeV γ -ray emission.

Table 1. Log of Suzaku observations.

Name	OBSID	Pointing direction		Observation start (UT)	Effective exposure (ks)	
		l	b		XIS	HXD-PIN
HESS J1614-South	503073010	331°2990	-0°7611	2008/09/20 18:18	53.7	40.9
HESS J1614-Center	503074010	331°4663	-0°6358	2008/09/21 13:31	47.7	43.0
HESS J1614-North*	501042010	331°5717	-0°5274	2006/09/15 16:00	44.5	-

* Matsumoto et al. 2008.

keV, respectively, while those for the BI sensor are defined as 0.3–3 keV and 3–7 keV, respectively. We excluded the corners of the CCD chips illuminated by the ^{55}Fe calibration sources. The images of the non-X-ray background (NXB) were generated using `xisnxbgen` (Tawa et al. 2008) and subtracted from the HESS J1614 images. Then, the soft- and hard-band images were divided by flat sky images simulated at 1.49 and 4.5 keV using the XRT+XIS simulator `xissim` (Ishisaki et al. 2007) for vignetting corrections. The images from the two FI sensors were summed and binned by a factor of 8.

The XIS FI images of the HESS J1614 region (HESS J1614-South and HESS J1614-Center) shown in figure 2 were smoothed using a Gaussian function with $\sigma = 0'.42$. The BI images were essentially the same, except for the poorer statistics. In the soft-band image, a

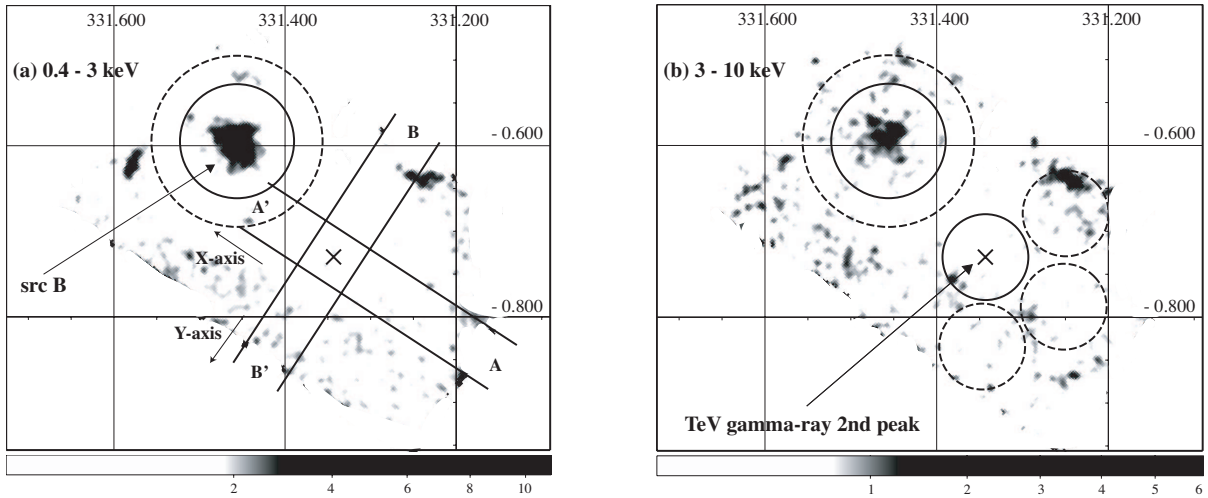


Fig. 2. Suzaku XIS FI (XIS 0+3) images of the HESS J1614 region (HESS J1614-South and HESS J1614-Center) in the Galactic coordinates: (a) 0.4–3 keV and (b) 3–10 keV bands. The images were smoothed using a Gaussian function with $\sigma = 0'.42$. A vignetting correction was applied after subtracting the NXB, as described in the text. The cross mark represents the position of the 2nd brightest peak of the TeV γ -ray emission. The solid lines in the left panel show the regions used for the photon count profiles shown in figure 3 (see section 3.1.1). The solid circle and the dashed circles in the right panel show the regions used for the determination of the upper limit to the X-ray emission (see section 3.2.1). The solid circle centered on src B is the integration region of source photons, and the dashed circle excluding the source region is that of background photons (see section 3.2.2).

bright X-ray object with a peak position of $(l, b) = (331^\circ45, -0^\circ59)$ ² was found. The position uncertainty, defined as a sigma of a Gaussian function obtained by fitting the projection of the object along the Galactic longitude, was $0'.4$. Thus, this object is coincident with Suzaku J1614–5152 (src B). Src B was also conspicuous in the hard-band image.

3.1.1. HESS J1614-South

There is no apparent X-ray structure suggesting an X-ray counterpart of the 2nd peak of the TeV γ -ray emission in either the soft- and hard-band images. To examine this quantitatively, we made photon count profiles along the strips AA' and BB' with a width of $3'.7$ in figure 2(a); the profiles are shown in figure 3. We see no systematic trend, consistent with the TeV γ -ray profile of HESS J1614-South described by a Gaussian function with $\sigma = 9'.0$ (Rowell et al. 2008), in either the soft and hard X-ray profiles. These profiles strengthen the absence of the X-ray counterpart corresponding to the 2nd peak of the TeV γ -ray emission.

3.1.2. HESS J1614-Center

We created the radial profile of src B and compared it with a point-spread function (PSF). The origin of the radial profile of src B was the peak of the X-ray emission. As for

² $(\alpha, \delta)_{J2000.0} = (16^h14^m04^s, -51^\circ52'27'')$.

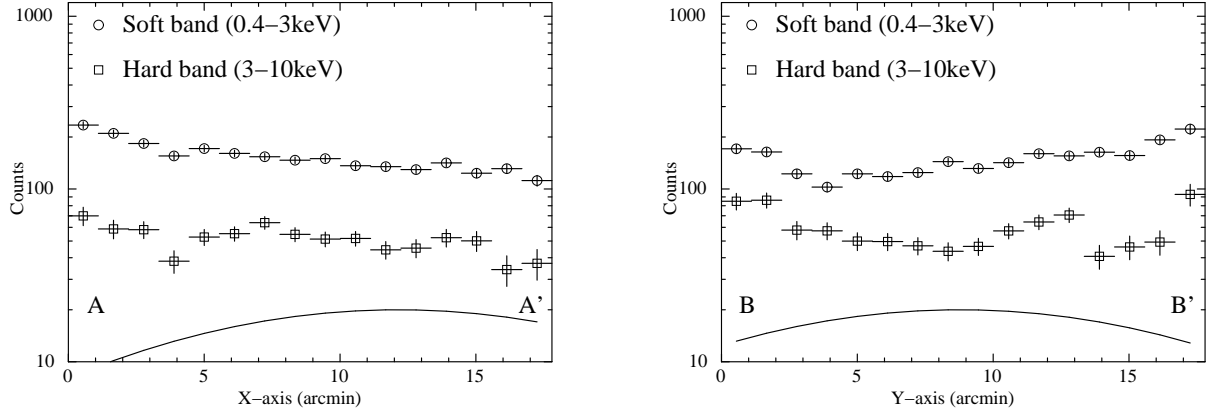


Fig. 3. Photon count profiles of the XIS images along the strips AA' (left) and BB' (right) shown in figure 2(a). The solid curve shows the Gaussian function of $\sigma = 9''.0$, which expresses the TeV γ -ray profile of HESS J1614-South.

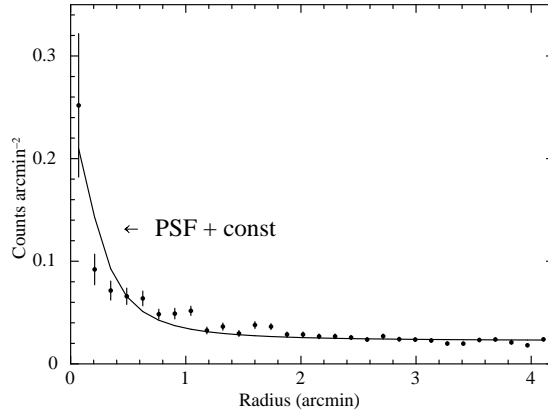


Fig. 4. Radial profile of src B extracted from the 3–10 keV band image of the XIS FI sensor (XIS 0+3). The solid line represents the XIS PSF profile with a constant component.

the PSF, we obtained the radial profile using the SS Cyg data observed on 2005 November 2 (OBSID=400006010), which are the verification phase data for the imaging capability of the XRT (Serlemitsos et al. 2007). Since the energy dependence of the PSF is negligible (Serlemitsos et al. 2007), the radial profile was extracted from the 0.4–10 keV band. In this analysis, NXB subtraction and vignetting correction were not applied to both the radial profile of src B and the PSF. Figure 4 shows the radial profile of src B in the 3–10 keV band. The profile cannot be fitted with the PSF plus a constant component model ($\chi^2/\text{d.o.f.} = 99.20/28$), and therefore src B must be an extended source or unresolved multiple sources.

3.2. XIS Spectrum

3.2.1. HESS J1614-South

There was no apparent X-ray counterpart corresponding to the 2nd peak of the TeV γ -ray emission, and we estimated the upper limit of the X-ray flux of this region. In order to determine the upper limit, we assumed a spectrum similar to src A; an absorbed power-law with the photon index $\Gamma = 2.0$ and the hydrogen-equivalent column density $N_{\text{H}} = 1.2 \times 10^{22} \text{ cm}^{-2}$ (Matsumoto et al. 2008). The cross sections of photoelectric absorption were obtained from Morrison & McCammon (1983).

We extracted the photons from the source region, the solid circle with a radius of $3'$ centered on the TeV γ -ray 2nd peak in figure 2(b), in the 2–10 keV band using the FI sensors (XISs 0 and 3). The number of the accumulated photons was 1111 ± 33 counts. Using three source-free regions surrounding the source region, the dashed circles around the TeV γ -ray 2nd peak in figure 2(b), we estimated the photons of the background emission. The number of the accumulated photons scaled the area to that of the source region was 1194 ± 35 counts. The exposure of the source was the same as that of the background. Thus, the number of the source minus background photons was -83 ± 48 counts, and the 3σ confidence upper limit on the photons in the source region was estimated to be 61 counts. Therefore, the 3σ confidence upper limit on the count rate in the source region was $1.1 \times 10^{-3} \text{ counts s}^{-1}$. Then, we calculated the flux upper limit with Redistribution Matrix Files (RMFs) and Ancillary Response Files (ARFs). We obtained RMFs using the `xisrmfgen`, and made ARFs for a flat emission with the `xissimarfgen` software (Ishisaki et al. 2007). The 3σ upper limit on the surface brightness is $5.6 \times 10^{-15} \text{ erg cm}^{-2} \text{ s}^{-1} \text{ arcmin}^{-2}$. Therefore, the upper limit on the flux from the circle of $3'$ radius (figure 2(b)) is $1.6 \times 10^{-13} \text{ erg cm}^{-2} \text{ s}^{-1}$.

3.2.2. HESS J1614-Center

A source region for src B is defined as the solid circle centered on src B in figure 2. We extracted light curves of src B in the soft- and hard-energy bands and found no significant time variability from them. Then, we extracted the XIS spectra of src B and subtracted background spectra. The source photons were extracted from the source region, whereas those of the background were extracted from the dashed circle excluding the source region (figure 2). We then combined the background-subtracted spectra obtained from the two FI sensors. We obtained RMFs and ARFs for a point source using the `xisrmfgen` and `xissimarfgen` software.

The spectra of src B are shown in figure 5. We fitted the spectra with an absorbed power-law model. The hydrogen-equivalent column density N_{H} , the photon index Γ , and the normalization were set to be free parameters. The best-fit parameters are $N_{\text{H}} = 1.1_{-0.1}^{+0.2} \times 10^{22} \text{ cm}^{-2}$ and $\Gamma = 3.2_{-0.2}^{+0.3}$. The best-fit χ^2 value is 103.47 for 128 degrees of freedom. The observed flux in the 2–10 keV band is $F(2\text{--}10 \text{ keV}) = 5.2 \times 10^{-13} \text{ erg cm}^{-2} \text{ s}^{-1}$.

We also tried fitting an absorbed blackbody model. The following are the best-fit parameters: $N_{\text{H}} = 0.29_{-0.09}^{+0.10} \times 10^{22} \text{ cm}^{-2}$ and $kT = 0.52_{-0.03}^{+0.04} \text{ keV}$. However, the best-fit χ^2 value of

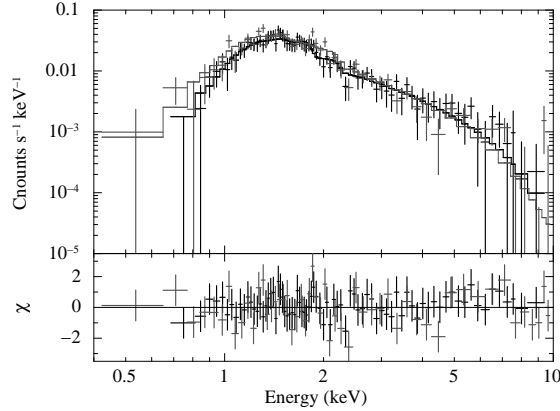


Fig. 5. XIS spectra of src B, shown with the best-fit power-law model. Black and gray lines represent the data and model for the XIS FI (XIS0+3) and XIS BI (XIS1), respectively.

169.24 for 128 degrees of freedom rejected the validity of the blackbody model at a confidence level of 99%.

3.3. HXD Data Analysis

We also analyzed the HXD-PIN data of HESS J1614-Center, which includes src B. The HXD-PIN spectrum of HESS J1614-Center was extracted after the selection of good time intervals. As for the selection, we made a new GTI by ANDing the GTI from the NXB file provided by the HXD team with the GTI in the screened event file. Dead-time correction was also applied to the extracted source spectrum. Since the NXB from charged particles modeled by the HXD team does not contain the cosmic X-ray background (CXB) component (Boldt 1987), we simulated the CXB for HESS J1614-Center following a recipe³ provided by the HXD team. We also used the response file for Epoch 5 provided by the HXD team. Note that the accuracy of the HXD-PIN background model was estimated to be less than 3% in the 15–40 keV range (Fukazawa et al. 2009).

The observed HXD-PIN count of HESS J1614-Center in the 15–40 keV band was 11559 ± 108 counts. The NXB and the simulated CXB count in the 15–40 keV band were 10432 ± 102 counts and 642 ± 25 counts, respectively. Thus, the observed HXD-PIN minus NXB+CXB count was 485 ± 150 counts. However, considering the accuracy of the HXD-PIN background model of 3%, the lower limit on the source count of HESS J1614-Center became 172 ± 151 counts, and the detection was at only 1.1σ . There are not enough net counts to study the HXD-PIN spectrum. We also searched a pulsation in the HXD-PIN data, but we did not detect any pulsation in the 15–40 keV band.

³ See http://heasarc.nasa.gov/docs/suzaku/analysis/pin_cxb.html.

3.4. XMM-Newton Analysis

The XMM-Newton observation of the HESS J1614 region was carried out from 2007 February 13 17:54 (UT) to February 14 03:07 (UT) (OBSID=0406550101), and this observation covered the HESS J1614-Center region with the EPIC instrument, which consists of one pn-type CCD camera (Strüder et al. 2001) and two MOS CCD cameras (Turner et al. 2001). In our Suzaku analysis, the radial profile of src B indicates that src B must be an extended source or unresolved multiple sources, and the light curves of src B do not show the time variability. The EPIC instrument provides a high spatial resolution, whose PSF (half energy width) is $\sim 15''$. Moreover, the time resolutions of each EPIC instrument are much better than the Suzaku/XIS (8 s), 73.4 ms for the pn and 2.6 s for the MOS in the full-frame mode. We therefore analyzed the XMM-Newton archival data.

The pn, MOS1 and MOS2 were operated in the standard full-frame mode using the medium filter. We used the Standard Analysis System (SAS) software version 10.0.0 for event selection. We selected the photons with the PATTERN of 0–4 for the pn and those of 0–12 for the MOS1 and MOS2, as valid X-ray events. We removed the time intervals in which the count rate in the 10–12 keV band within the entire field of view was higher than $0.25 \text{ counts s}^{-1}$ for the pn and $0.20 \text{ counts s}^{-1}$ for the MOS1 and MOS2, since such events are considered to be a rapid increase in the background induced by soft protons. The resultant exposure time was 1 ks for the pn and 10 ks for the MOS1 and MOS2. Since the photon statistics were poor for the pn, we did not use the pn data in this analysis.

3.4.1. Image Analysis

Figure 6 shows the combined MOS1 and MOS2 image in the 0.4–10 keV band. We found several sources within the source and background regions of src B used to create the XIS spectra. We therefore searched for X-ray point sources using the source detection task `edetect_chain` in the SAS software package. We set the lower threshold of maximum likelihood method used in `edetect_chain` to be 10 (corresponding roughly to 4σ detection). The detected point sources in the 0.4–10 keV band are shown with thick open circles in figure 6. Four point sources were detected in the XIS source region for src B, while only one point source was detected in the XIS background region for src B. We designated these objects as XMMU J161406.0–515225 (src B1), XMMU J161409.3–515213 (src B2), XMMU J161409.8–515352 (src B3), XMMU J161414.1–514857 (src B4), and XMMU J161426.8–515705 (src B5). For each point source, we accumulated photons from a circular region with a radius of $15''$, and then estimated their count rates. Table 2 summarizes the count rates of these detected point sources. We also gave the count rates of the XIS source and background regions for src B excluding the point sources in order to indicate the count rate of the background photons in this field. The count rate of src B1 is higher than the other sources by a factor of ~ 5 . Moreover, the peak position of src

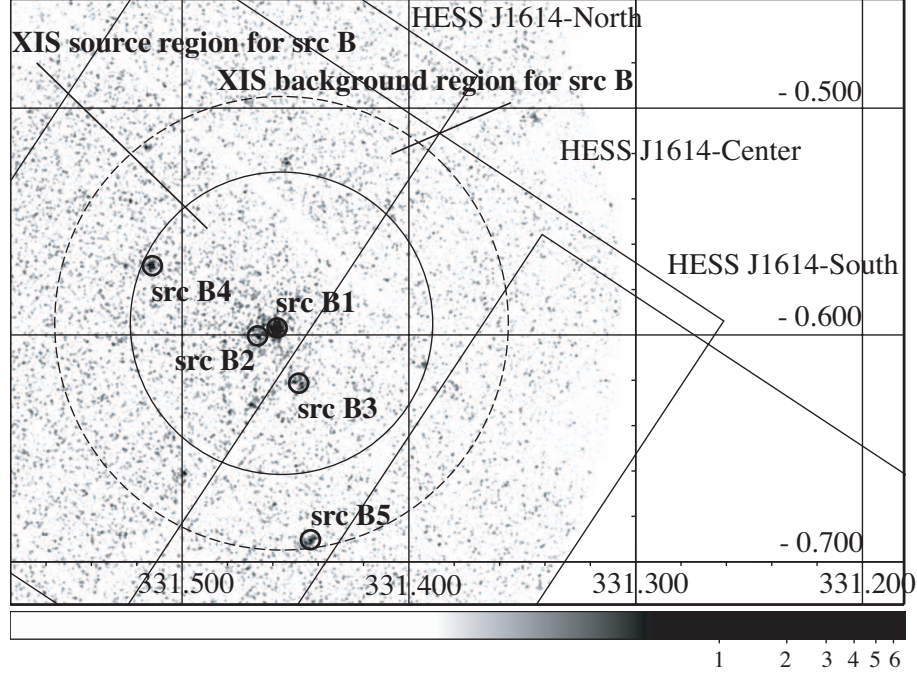


Fig. 6. MOS 1+2 zoomed image in the 0.4–10 keV band including the XIS source (solid circle) and background (dashed circle excluding the source region) regions for src B. The solid squares represent the Suzaku/XIS field of views of the HESS J1614-North/HESS J1614-Center/HESS J1614-South observations. We also show the extraction regions for the detected point sources, which are used to estimate the source count rates, with thick open circles. Lines of constant Galactic latitude and longitude are plotted and labeled in the interior of the figure.

B1, $(l, b) = (331.45, -0.59)$ ⁴ with the position uncertainty of $2''.8$, is consistent with that of Suzaku src B. These indicate that Suzaku src B is multiple sources and the main object is src B1.

Figure 7 shows the radial profile of src B1 extracted from the MOS detectors in the 1.2–2.4 keV band; The origin of the radial profile was the peak of the X-ray emission, and NXB subtraction and vignetting correction were not applied to it. Then, we compared it with a point-spread function (PSF) in order to investigate whether or not src B1 is a point source. Since the PSF of the XMM-Newton telescopes depends on the energy, we used the PSF at an energy of 1.8 keV. We parameterized the PSF at 1.8 keV with a King-type function: $\text{PSF}(r) = A(1 + (r/r_c)^2)^\alpha$, where A is a normalization, $r_c = 4''.36$ is a core radius and $\alpha = -1.41$ is a slope (see the XMM-SOC-CAL-TN-0022 and XMM-SOC-CAL-TN-0029 documents online at <http://xmm.vilspa.esa.es>). We fitted the radial profile in the range of $0''.1 < r < 200''$ with the above PSF model plus constant which represents the background. In this fit, the normalization and the constant were free. We overlaid the best-fit model on the radial profile in figure 7. The best-fit χ^2 value is 109.6 for 98 degrees of freedom. This result suggests that src B1 is a point

⁴ $(\alpha, \delta)_{\text{J2000.0}} = (16^{\text{h}}14^{\text{m}}06^{\text{s}}, -51^{\circ}52'25'')$.

Table 2. Count rates of XMM-Newton data.

Region	R.A. (J2000.0)	Decl. (J2000.0)	Count rate*		
			[10^{-3} counts s^{-1}]		
			0.4 – 3 keV	3 – 10 keV	Total
src B1 [†]	16 14 06	−51 52 25	22.7±1.0	2.03±0.31	24.7±1.1
src B2 [†]	16 14 09	−51 52 13	4.70±0.48	0.629±0.175	5.33±0.51
src B3 [†]	16 14 09	−51 53 52	3.59±0.42	0.437±0.146	4.03±0.44
src B4 [†]	16 14 14	−51 48 57	4.66±0.48	0.776±0.194	5.43±0.51
src B5 [†]	16 14 26	−51 57 05	3.83±0.43	0.242±0.108	4.08±0.44
XIS source region – (src B1 + src B2 + src B3 + src B4) [‡]			0.670±0.011	0.405±0.009	1.07±0.01
XIS background region – src B5 [‡]			0.563±0.009	0.377±0.008	0.940±0.012

* All errors are at the 1σ confidence level.

[†] Extraction regions are the circle with a radius of $15''$.

[‡] Extraction regions are scaled to the circle with a radius of $15''$.

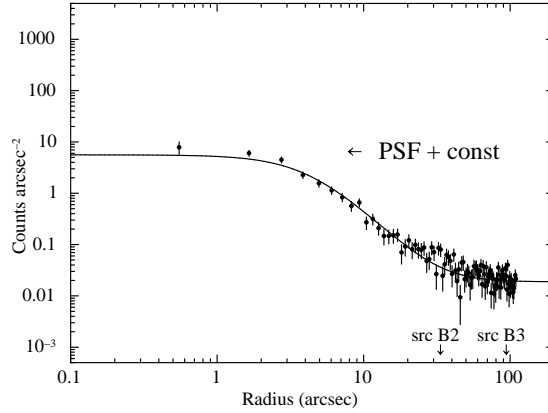


Fig. 7. Radial profile of src B1 extracted from the MOS detectors in the 1.2–2.4 keV band. The solid line represents the PSF profile with a constant component. The downward arrows represent the positions of src B2 and src B3 (see figure 6)

source.

3.4.2. Spectral Analysis

In order to check for consistency with the Suzaku results, we extracted the MOS spectra of the XIS source region for src B and subtracted the background spectra of the XIS background region for src B (figure 6). We fitted the spectra with an absorbed power-law model. The fit is acceptable with the best-fit χ^2 value of 47.98 for 65 degrees of freedom. The best-fit parameters are $N_H = 1.1^{+0.4}_{-0.3} \times 10^{22} \text{ cm}^{-2}$ and $\Gamma = 3.0^{+0.6}_{-0.5}$. The observed flux in the 2–10 keV band is $F(2\text{--}10 \text{ keV}) = 6.9 \times 10^{-13} \text{ erg cm}^{-2} \text{ s}^{-1}$. Figure 8 shows the background-subtracted spectra together with the best-fit model and the fit residuals. The best-fit results of Suzaku src B and XMM-

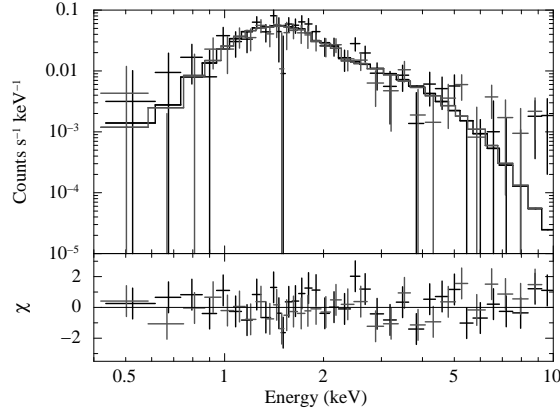


Fig. 8. MOS1 (black) and MOS2 (grey) spectra of src B. The data and their best-fit power-law model are represented by cross marks and solid lines, respectively.

Newton src B are summarized in table 3. The best-fit parameters of src B are consistent with Suzaku and XMM-Newton. The X-ray flux of XMM-Newton is $\sim 30\%$ larger than that of Suzaku, and this may indicate time variability.

Table 3. Best-fit results of the X-ray spectra.*

	Suzaku src B	XMM-Newton src B	XMM-Newton src B1	
Model [†]	PL	PL	PL	BB
N_{H} (10^{22}cm^{-2})	$1.1^{+0.2}_{-0.1}$	$1.1^{+0.4}_{-0.3}$	$2.4^{+0.4}_{-0.4}$	$1.1^{+0.3}_{-0.2}$
$\Gamma/(kT)$ (keV)	$3.2^{+0.3}_{-0.2}$	$3.0^{+0.6}_{-0.5}$	$5.2^{+0.6}_{-0.5}$	$0.38^{+0.04}_{-0.04}$
$F_{2-10\text{keV}}^{\text{obs}\ddagger}$	5.2	6.9	1.7	1.5
$F_{2-10\text{keV}}^{\text{abscor}\S}$	6.1	8.0	2.8	2.0
$\chi^2/\text{d.o.f.}$	103.47/128	47.98/65	21.98/25	24.91/25

* Errors are at the 90% confidence level.

[†] Model used for the spectral fitting: "PL" is a power-law model, and "BB" is a blackbody model.

[‡] Observed flux in the 2–10 keV band in units of $10^{-13} \text{ erg cm}^{-2} \text{ s}^{-1}$.

[§] Absorption corrected flux in the 2–10 keV band in units of $10^{-13} \text{ erg cm}^{-2} \text{ s}^{-1}$.

Then, we extracted the MOS spectra of src B1. The circle with a radius of $20''$ centered on src B1 was the extraction region of the source photons, whereas the XIS background region for src B excluding the circle with a radius of $20''$ centered on src B5 was that of the background photons (figure 6). The spectra of src B1 are shown in figure 9. We fitted the spectra with an absorbed power-law model. The best-fit parameters are $N_{\text{H}} = 2.4^{+0.4}_{-0.4} \times 10^{22} \text{ cm}^{-2}$ and $\Gamma = 5.2^{+0.6}_{-0.5}$. We also tried to fit the spectra by an absorbed blackbody model. The best-fit parameters are as follows: $N_{\text{H}} = 1.1^{+0.3}_{-0.2} \times 10^{22} \text{ cm}^{-2}$ and $kT = 0.38^{+0.04}_{-0.04} \text{ keV}$. The best-fit parameters of the power-law and blackbody models are listed in table 3. Moreover, we tried fitting a thermal

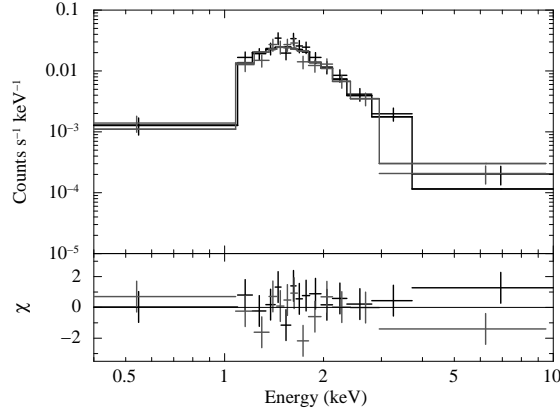


Fig. 9. MOS1 (black) and MOS2 (grey) spectra of src B1. The data and their best-fit power-law model are represented by cross marks and solid lines, respectively.

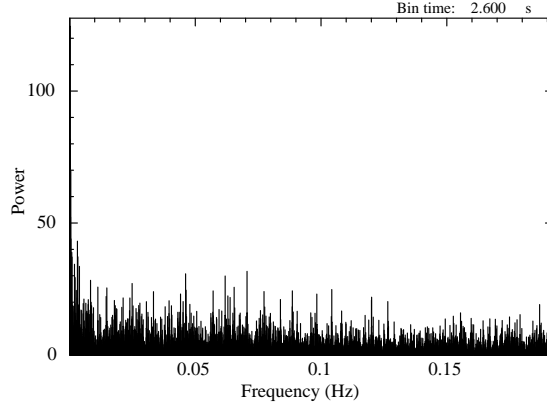


Fig. 10. Power spectrum of src B1 in the 1–5 keV band with the time bin size of 2.6 s for the MOS data.

plasma model (the MEKAL model: Mewe et al. 1985). However, the thermal model yielded an abundance of zero (< 0.044) solar, which is an extremely low abundance, and therefore is not realistic. Since the statistics were poor, it was impossible to study the spectra of the other sources.

3.4.3. Timing Analysis

We carried out a timing analysis of src B1. Since there was nearly no source flux below ~ 1 keV and above ~ 5 keV, we searched a pulsation in the 1–5 keV band for the MOS data. After barycentric correction to the event file, we created the light curve of src B1 with the minimum time resolution (2.6 s). The power spectrum on the basis of the combined MOS1 and MOS2 light curve in the 1–5 keV band is shown in figure 10. We did not detect a pulsation of src B1 for the MOS data.

4. Discussion

4.1. The TeV-to-X-ray flux ratio of HESS J1614

HESS J1614 has two regions with intense γ -ray emission. The γ -ray spectrum yields $\Gamma = 2.46$ and the flux in the 1–10 TeV band from a circular region with a radius of 0.4° is estimated to be $1.8 \times 10^{-11} \text{ erg cm}^{-2} \text{ s}^{-1}$ (Aharonian et al. 2006). Matsumoto et al. (2008) found the hard extended emission, Suzaku src A, at the position of the 1st brightest peak of the TeV γ -ray emission, as the best candidate for the X-ray counterpart of HESS J1614; the best-fit parameters are $N_{\text{H}} = 1.2_{-0.4}^{+0.5} \times 10^{22} \text{ cm}^{-2}$ and $\Gamma = 1.7_{-0.3}^{+0.3}$, and the flux of Suzaku src A in the 2–10 keV band is $F(2\text{--}10 \text{ keV}) = 5.3 \times 10^{-13} \text{ erg cm}^{-2} \text{ s}^{-1}$. Additionally, we reveal that there is no evidence for the X-ray emission at the position of the 2nd brightest peak of the TeV γ -ray emission; the XIS sets the stringent upper limit of $1.6 \times 10^{-13} \text{ erg cm}^{-2} \text{ s}^{-1}$ in the 2–10 keV band. As a result, the X-ray counterpart to the TeV γ -ray emission is just Suzaku src A. Therefore, it is ensured that the flux ratio $F(1\text{--}10 \text{ TeV})/F(2\text{--}10 \text{ keV})$ of HESS J1614 is ~ 34 , which is still one of the largest values observed among extended VHE objects (see Matsumoto et al. 2007 and references therein).

4.2. The nature of HESS J1614

XMM-Newton src B1 is located at the middle of HESS J1614. Within the error circle of XMM-Newton src B1, there is an infrared source, 2MASS J16140610–5152264, at $(l, b) = (331.4579, -0.5973)$. The X-ray spectrum of XMM-Newton src B1 is described using a power-law model with $\Gamma = 5.2_{-0.5}^{+0.6}$ or a blackbody model with $kT = 0.38_{-0.04}^{+0.04} \text{ keV}$. The best-fit column densities of both models are different by a factor of ~ 2 . The best-fit column density of the power-law model is almost the same as the total Galactic HI column density towards the HESS J1614 region ($\sim 2.2 \times 10^{22} \text{ cm}^{-2}$; Dickey & Lockman 1990), while that of the blackbody model is approximately equal to half of it. On the other hand, the best-fit column density of the power-law model is about twice larger than that of Suzaku src A, while that of the blackbody model is almost the same as that of Suzaku src A. If we assume the blackbody emission, XMM-Newton src B1 may be at about the same distance to Suzaku src A and may also be physically related to HESS J1614.

An object which shows a soft X-ray spectrum like XMM-Newton src B1 includes an anomalous X-ray pulsar (AXP : Mereghetti 2008). The spectra of AXPs are described by steep power laws ($\Gamma > 3$) and/or blackbody models with low temperature ($kT \leq 0.5 \text{ keV}$). AXPs often show time variability with a period of 2–12 s. However, no such variability was found from XMM-Newton src B1.

If XMM-Newton src B1 is related to Suzaku src A and HESS J1614, the nature of HESS J1614 is similar to that of CTB37B (Nakamura et al. 2009). CTB37B is an SNR which has the diffuse non-thermal power-law component ($\Gamma \sim 1.5$) at the position of the TeV γ -ray emission.

Moreover, the point source which shows the soft spectrum considered to be an AXP was found at the offset position of the TeV γ -ray emission (Nakamura et al. 2009; Sato et al. 2010). Thus, if XMM-Newton src B1 is an AXP, HESS J1614 may be an SNR associated with an AXP. In that case, it is considered that XMM-Newton src B1 is an AXP produced by a supernova explosion, and a shocked region in the SNR can be seen as Suzaku src A. The approximate radius of HESS J1614 ($r \sim 10' = 30$ pc @ 10 kpc) suggests that HESS J1614 may be an SNR with an age of $\sim 10^5$ yrs (Padmanabhan 2001). Yamazaki et al. (2006) suggested that the ratio of TeV γ -ray to X-ray energy flux of old SNRs with an age of $\sim 10^5$ yr could be very large, in some instances more than ~ 100 . The flux ratio of HESS J1614 is in agreement with this scenario. Here, we assume the distance to HESS J1614 is 10 kpc, since the best-fit column density of the blackbody model which is almost the same as that of Suzaku src A, is approximately equal to half of the total Galactic HI column density towards the HESS J1614 region. Assuming a distance of 10 kpc, the luminosities of XMM-Newton src B1 in the 2–10 keV band are 3×10^{33} erg s $^{-1}$ for the power-law model and 2×10^{33} erg s $^{-1}$ for the blackbody model. These luminosities are consistent with that of AXPs (e.g., The McGill SGR/AXP Online Catalog.⁵). Meanwhile, assuming a distance of 10 kpc, the luminosity of Suzaku src A in the 2–10 keV band is 6×10^{33} erg s $^{-1}$ (Matsumoto et al. 2008). This luminosity is smaller than the synchrotron X-ray luminosity of young SNRs (e.g., Dyer et al. 2004).

On the other hand, Rowell et al. (2008) suggested the relation between HESS J1614 and Pismis 22. Pismis 22 is an open cluster characterized by the following cluster fundamental parameters: $E(B-V)$ color excess = 2.00 ± 0.10 mag, distance = 1.0 ± 0.4 kpc and Age = 40 ± 15 Myr (Piatti et al. 2000). Rowell et al. (2008) pointed out that Pismis 22 may easily account for the TeV luminosity if the cluster has a stellar wind luminosity of ten B-type stars and 20% of the stellar wind kinetic energy is converted to the γ -ray. The size of Pismis 22 is $4.0'$, it is conceivable that XMM-Newton src B1 is within this cluster. However, according to the best-fit column densities of both models, the distance to XMM-Newton src B1 of 1.0 kpc is too close. Moreover, the spectrum of XMM-Newton src B1 cannot be described by the optically thin thermal plasma model seen from some O and B-type stars (Colombo et al. 2007). There are other TeV γ -ray sources, such as Cyg-OB2 (TeV J2032+4130), suspected the relation with the open cluster (Aharonian et al. 2002). However, in the case of TeV J2032+4130, the size of the extended X-ray emission is similar to that of the TeV γ -ray emission (Horns et al. 2007). Thus there are some differences with HESS J1614.

5. Summary

We observed the south and center regions of HESS J1614 with Suzaku. There was no positive detection at the 2nd peak position, and we set an upper limit of 1.6×10^{-13} erg cm $^{-2}$ s $^{-1}$

⁵ See (<http://www.physics.mcgill.ca/~pulsar/magnetar/main.html>).

to the 2–10 keV band flux. The high value of $f_{\text{TeV}}/f_X \sim 34$ may suggest that HESS J1614 is a proton accelerator. We also detected the soft X-ray source, Suzaku J1614–5152 (Suzaku src B), at the middle of HESS J1614. Using the XMM-Newton archival data, we revealed that Suzaku src B consists of multiple point sources. The brightest point source, XMMU J161406.0–515225 (XMM-Newton src B1), shows a soft X-ray spectrum. XMM-Newton src B1 might be an AXP and may be physically related to Suzaku J1614–5141 (Suzaku src A), which was found at the 1st peak position in the previous observation.

The authors are grateful to Professors W. Hoffman and S. Funk for kindly providing the HESS image. We thank H. Kunieda, K. Ishibashi, A. Furuzawa, and H. Mori for their useful comments. We also thank all Suzaku members. MS is supported by Grant-in-Aid for Japan Society for the Promotion of Science (JSPS) Fellows, 235737. HM is supported by Grant-in-Aid for Scientific Research (B), 22340046. This work was partially supported by the Grant-in-Aid for Nagoya University Global COE Program, "Quest for Fundamental Principles in the Universe: from Particles to the Solar System and the Cosmos", from the Ministry of Education, Culture, Sports, Science and Technology of Japan.

References

- Aharonian, F., et al. 2002, *A&A*, 393, L37
 Aharonian, F., et al. 2005a, *Science*, 307, 1938
 Aharonian, F., et al. 2005b, *A&A*, 442, 1
 Aharonian, F., et al. 2006, *ApJ*, 636, 777
 Aharonian, F., et al. 2008, *A&A*, 490, 685
 Boldt, E. 1987, in *IAU symp. 124, Observational Cosmology*, ed. A. Hewitt, G. Burbidge, & L. Z. Fang (Dordrecht: Reidel), 611
 Albacete Colombo, J. F., Flaccomio, E., Micela, G., Sciortino, S., & Damiani, F. 2007, *A&A*, 464, 211
 Dickey, J. M., & Lockman, F. J. 1990, *ARA&A*, 28, 215
 Dyer, K. K., Reynolds, S. P., & Borkowski, K. J. 2004, *ApJ*, 600, 752
 Fukazawa, Y., et al. 2009, *PASJ*, 61, S17
 Hess, V. F. 1912, *Phys. Zeits.*, 13, 1084
 Horns, D., Hoffmann, A. I. D., Santangelo, A., Aharonian, F. A., & Rowell, G. P. 2007, *A&A*, 469, L17
 Ishisaki, Y., et al. 2007, *PASJ*, 59, S113
 Kokubun, M., et al. 2007, *PASJ*, 59, S53
 Koyama, K., Petre, R., Gotthelf, E. V., Hwang, U., Matsuura, M., Ozaki, M., & Holt, S. S. 1995, *Nature*, 378, 255
 Koyama, K., et al. 2007, *PASJ*, 59, S23
 Matsumoto, H., et al. 2007, *PASJ*, 59, S199
 Matsumoto, H., et al. 2008, *PASJ*, 60, S163

- Mereghetti, S. 2008, *A&A Rev.*, 15, 225
- Mewe, R., Gronenschild, E. H. B. M., & van den Oord, G. H. J. 1985, *A&AS*, 62, 197
- Mitsuda, K., et al. 2007, *PASJ*, 59, 1
- Morrison, R., & McCammon, D. 1983, *ApJ*, 270, 119
- Nakamura, R., Bamba, A., & Ishida, M. 2009, *PASJ*, 61, S197
- Padmanabhan, P. 2001, *Theoretical astrophysics. Vol. II: Stars and Stellar Systems*. Cambridge University Press, Cambridge, MA
- Piatti, A. E., Claria, J. J., & Bica, E. 2000, *A&A*, 360, 529
- Renaud, M., Hoppe, S., Komin, N., Moulin, E., Marandon, V., & Clapson, A.-C. 2008, *AIP Conf. Series*, 1085, 285
- Rowell, G., Horns, D., Fukui, Y., & Moriguchi, Y. 2008, *AIP Conf. Series*, 1085, 241
- Sato, T., Bamba, A., Nakamura, R., & Ishida, M. 2010, *PASJ*, 62, L33
- Serlemitsos, P. J., et al. 2007, *PASJ*, 59, S9
- Strüder, L., et al. 2001, *A&A*, 365, L18
- Takahashi, T., et al. 2007, *PASJ*, 59, S35
- Tawa, N., et al. 2008, *PASJ*, 60, S11
- Turner, M. J. L., et al. 2001, *A&A*, 365, L27
- Uchiyama, Y., et al. 2008, *PASJ*, 60, S35
- Uchiyama, H., et al. 2009, *PASJ*, 61, S9
- Yamazaki, R., Kohri, K., Bamba, A., Yoshida, T., Tsuribe, T., & Takahara, F. 2006, *MNRAS*, 371, 1975